

Oscillatory shear flows of dense suspensions at imposed pressure: Rheology and microstructure

Junhao Dong¹ and Martin Trulsson^{1, a)}

Theoretical Chemistry, Department of Chemistry, Lund University, Sweden

(Dated: 15 June 2021)

Oscillatory shear has been widely used to study the rheological properties of suspensions under unsteady shear. Furthermore, recent works have shown that oscillatory flows can improve the flowability of dense suspensions. While most studies have been done under constant volume, we here study oscillatory shear flows of two-dimensional suspensions using a normal pressure-controlled set-up. To characterise the rheology, we introduce both a complex macroscopic friction coefficient μ^* , following the convention of the complex viscosity η^* , and a shear-rate averaged viscous number J' . The rheology and microstructure of dense suspensions are studied by systematically varying the strain magnitude γ_0 and J' using numerical simulations. We study both suspensions composed of frictional ($\mu_p = 0.4$) or frictionless ($\mu_p = 0$) particles and find that the critical values, as $J' \rightarrow 0$, of both the complex macroscopic friction and the number of total and sliding contacts decrease with decreasing γ_0 . For suspensions composed of frictional particles, we also find that the critical (*i.e.*, the shear jamming) packing fraction ϕ_c increase with decreasing γ_0 . In both cases, frictional and frictionless, we find that the rheological response approaching the shear jamming turns from a viscous to an elastic response as γ_0 is lowered below ~ 0.33 .

I. INTRODUCTION

Oscillatory shear measurements are widely used when studying mechanical properties (such as viscosity and elasticity) of soft materials and complex fluids such as suspensions, emulsions, polymer melts[1–3]. In a typical oscillatory shear measurement, the material is subject to an oscillating shear-rate, *i.e.* $\dot{\gamma} = \dot{\gamma}_0 \cos(\omega t)$, or equivalently an oscillating strain, *i.e.* $\gamma = \gamma_0 \sin(\omega t)$, of frequency $\frac{\omega}{2\pi}$ and with magnitudes equal to $\dot{\gamma}_0 = \gamma_0 \omega$ during which the mechanical response is monitored as a function of time. For a purely viscous material, the mechanical response will always be in-phase with the applied shear-rate; while for a purely elastic material the mechanical response will be in-phase with the applied strain (and out-of-phase with the applied shear-rate). In many cases, the tested materials are viscoelastic, which means that the mechanical response contains both in-phase and out-of-phase parts with respect to the shear-rate (or strain). The viscoelastic response is usually quantified by the elastic storage modulus G' and the viscous loss modulus G'' , or equivalently by the imaginary part of the complex viscosity η'' and the real part of the complex viscosity η' . The former one accounts for the mechanical response that is in-phase with the strain, and the latter one accounts for the part that is in-phase with the shear-rate[4].

The rheology of non-Brownian non-inertial dense suspensions composed of hard particles at steady shear (*i.e.*, at a constant shear-rate $\dot{\gamma}$) can be characterised by one single dimensionless parameter: the viscous number $J = \eta_f \dot{\gamma} / P$ [5], where P is the pressure (normal

stress) and η_f the interstitial fluid viscosity. This characterisation assumes that the interstitial fluid is viscous enough such that particle inertia can be ignored. Both the packing fraction ϕ and the macroscopic friction (or stress ratio) $\mu = \sigma / P$, σ being the shear stress, can then be described by two single-variable constitutive relationships: $\phi = \phi(J)$ and $\mu = \mu(J)$ [5–7]. For non-Brownian dense suspensions, one is typically interested in how the rescaled viscosity $\eta / \eta_f (= \mu / J)$ varies with the packing fraction of the solid material ϕ (which is experimentally more accessible than J). The divergence of the viscosity from below the shear jamming packing fraction ϕ_c is found empirically (or semi-empirically) to follow a power-law as $\eta / \eta_f \sim (\phi_c - \phi)^{-n}$, where n is a positive exponent and usually close to two[5 and 8]. However, the values of ϕ_c do depend on several factors, for example, the shape of the particles[9], the type of interactions between the particles[10], the dimensionality of the system[11], and the particle-particle friction[7 and 12]. A key result from above analysis is that the viscosity of a non-Brownian non-inertial suspensions is shear-rate-independent for a given fixed packing fraction.

Things do, in general, become more complicated under unsteady conditions, so also for suspensions subjected to oscillatory shear flows [13]. Oscillatory shear introduces both a frequency and a magnitude into the rheological response. Traditionally and depending on the strain magnitude, the oscillatory shear flows are usually characterised into a Small Amplitude Oscillatory Shear (SAOS)-regime and a Large Amplitude Oscillatory Shear (LAOS)-regime. Such studies are usually carried out under constant packing fraction. In the SAOS-regime, all stresses show linear response, and one is effectively scanning a material's linear viscoelastic properties[14 and 15]. The LAOS-regime is characterised as the non-linear regime, where stresses deviate from simple

^{a)}Electronic mail: martin.trulsson@teokem.lu.se

linear responses[4, 16–20]. The non-linearity in LAOS is often measured using Fourier Transformation[4, 20, and 21] or Chebyshev polynomial decomposition[19 and 22] in frequencies, and is far from trivial to analyse.

LAOS has been used to study complex behaviors of various suspensions. For example, it is used to probe microstructure and rheology of thixotropic suspensions composed of colloidal particles [23 and 24]. LAOS can, furthermore, be used to yield glassy hard sphere colloidal suspensions, where the suspension is doing a transition from a Brownian to an effectively non-Brownian suspension [25], characterised by a high Péclet number. In our work, we deal with an idealised non-inertial non-Brownian suspensions, corresponding to having an infinite Péclet number, and due to the fact that the rheology is rate-independent, the final quantities will have zero frequency dependencies. This simplifies the analysis considerably as one only need to account for the magnitude.

Besides studying the rheology of dense suspensions in oscillatory shear, it has found to be insightful to look at the microstructure, *e.g.*, how the number of particle contacts evolves [26]. It has found that if one instantaneously reverses the direction of the shear, the viscosity of the suspension will first drop and then gradually increase back to its steady-shear value[27–29]. Such behaviour is explained by the breakage and re-establishment of the contacts between the particles in a suspension. Oscillatory shear flows at large strain magnitudes can be considered as a series of shear reversals from a steady shear[30]. As the strain magnitude is lowered, the particles in the suspensions cannot fully restore the same microstructure as found at steady shear[31], yielding a lower viscosity. It has been shown that if the strain magnitude is small enough, the trajectories of the particles in the suspensions can become fully reversible, indicating that the suspensions reach an “absorbing” state where the particles self-organised to avoid each other[32–35].

Moreover, some recent studies have found that by applying an oscillatory shear perpendicular to a primary stationary shear, one can reduce the viscosity of the suspension[31 and 36] and, in some cases, even “unjam” suspensions that have been jammed by steady shear[35]. A possible explanation of this is that the perpendicular oscillation tilts and eventually breaks the force chains in the suspensions[36]. In our previous work[37], we found that for a two-dimensional system, an oscillatory shear parallel to the primary can also decrease the viscosity of a dense suspension, illustrating that the viscosity reduction is primarily due to a general restructuring of the microstructure. We further showed that the shear-jamming packing fractions were pushed to higher values for small oscillatory strains for suspensions composed of frictional particles but not for frictionless.

In this work, we continue our previous study[37] and present additional numerical results on the rheology on non-Brownian dense suspensions of hard particles immersed in a Newtonian fluid under oscillatory shear in a pressure-controlled set-up. Our new results show that dense suspensions have a viscoelastic response if the oscillatory strain magnitudes are small enough (typically below 0.33). At the same conditions, we find that the critical values of the complex macroscopic friction $|\mu^*|_c$ and the number of contacts Z_c (as $\dot{\gamma} \rightarrow 0$ or $P \rightarrow \infty$) saturate to values significantly below the steady shear ones. These changes are attributed to an altered microstructure at small strain magnitudes compared to steady shear.

II. SIMULATION METHODS

We study dense suspensions in two dimensions consisting of ~ 1000 polydisperse circular discs, with an average diameter equal to d , using a discrete element method. The particles of the suspensions are confined between two rough walls, which both are exposed to a constant imposed pressure P^{ext} in the normal direction (now denoted the y -direction) and a relative oscillatory velocity difference between them along the x -axis (*i.e.* the tangential direction), the latter resulting in a macroscopic shear-rate $\dot{\gamma}(t) = \dot{\gamma}_0 \cos(\omega t)$, where $\dot{\gamma}_0$ is the magnitude of the oscillatory shear and $\omega/2\pi$ the frequency of the oscillations. The strain is then given as $\gamma(t) = \gamma_0 \sin(\omega t)$ with the strain magnitude of the oscillations $\gamma_0 = \dot{\gamma}_0/\omega$ (corresponding to the maximum strain in one direction). The walls are constructed by fusing the same kind of discs as compose the flowing discs. Interactions between discs are described by harmonic springs[38]

$$\mathbf{f}_{ij} = k_n \delta_n^{ij} \mathbf{n}^{ij} + k_t \delta_t^{ij} \mathbf{t}^{ij}, \quad (1)$$

where k_n is the normal spring constant, $k_t = k_n/2$ the tangential spring constant, δ_n^{ij} the normal overlap, and δ_t^{ij} the tangential displacement. The ratio between the normal spring constant and the imposed pressure k_n/P^{ext} is kept equal to $3 \cdot 10^4$ to ensure a near-hard disc condition. Each tangential force is restricted by a Coulomb friction criterion, $|f_t^{ij}| \leq \mu_p |f_n^{ij}|$, where the particle-particle friction coefficient was chosen to be either $\mu_p = 0.4$ (frictional) or 0 (frictionless). The discs are also subject to both viscous drag and torque, given as

$$\mathbf{f}_i^v = \frac{3\pi\eta_f}{1 - \phi_0} [\mathbf{u}^f(y) - \mathbf{u}_i], \quad (2)$$

$$\tau_i^v = \frac{\pi\eta_f d^2}{1 - \phi_0} [\omega^f - \omega_i], \quad (3)$$

with $\phi_0 = 0.76$ being a typical packing fraction, and where \mathbf{u}_i and ω_i are the translational and angular velocities of disc i , $\mathbf{u}^f(y) = (\dot{\gamma}y, 0)$ the interstitial fluid velocity where y is the y -coordinate of disc i , and $\omega^f = \dot{\gamma}/2$ the fluid

angular velocity (vorticity). Both simulations with and without lubrication forces and torques were considered. In the case of simulations with lubrication forces, the disc dynamics is described by Newtonian dynamics, where we set the maximum Stokes number $St = \rho \dot{\gamma}_0 d^2 / \eta_f$ smaller than 0.4 so that there are negligible inertial effects. The results of simulations with lubrication force are presented in section I in the SI, where we show that including lubrication forces gives similar results compared to the results without lubrication forces. In the case of simulations without lubrication forces, the disc dynamics is strictly overdamped and given by a force and a torque balance

$$\mathbf{f}_i^{ext} + \mathbf{f}_i^v = - \sum_j \mathbf{f}_{ij}, \quad (4)$$

$$\tau_i^{ext} + \tau_i^v = - \sum_j \tau_{ij}, \quad (5)$$

on each disc and where \mathbf{f}_i^{ext} , \mathbf{f}_i^v and \mathbf{f}_{ij} are the external, viscous and contact forces respectively and τ_i^{ext} , τ_i^v and τ_{ij} the corresponding torques. In the overdamped simulations, we used a time-step equal to a tenth of the characteristic time-scale $t_0 = \frac{3\pi\eta_f}{(1-\phi_0)k_n}$.

For each simulation, we fix the confining pressure P^{ext} , the magnitude of oscillatory shear $\dot{\gamma}_0$ and the oscillation frequency ω . The suspensions are ‘‘pre-equilibrated’’ before any properties are measured, such as to avoid drift and transient behaviours. We accumulated statistics over a minimum of 10 absolute strains ($\int |\dot{\gamma}| dt \geq 10$) and at least one full oscillation period (for the largest γ_0). All reported quantities are measured by excluding the first five layers close to each wall to eliminate boundary effects. Sampling frequency was put equal to 60 measures (evenly distributed in time) per oscillation. In the following, we only report the particle contact and lubrication stresses, ignoring the stress coming from the interstitial fluid itself ($\sigma_{fluid} = \eta_f \dot{\gamma}$).

III. SUSPENSIONS RHEOLOGY

For suspensions subjected to oscillatory shear, the shear stress σ can consist of contributions from both elastic and viscous responses. In the linear response regime, the shear stress can be written as[3 and 39]

$$\sigma = G' \gamma(t) + \frac{G''}{\omega} \dot{\gamma}(t) = \eta' \dot{\gamma}_0 \sin(\omega t) + \eta'' \dot{\gamma}_0 \cos(\omega t), \quad (6)$$

where G' is the storage modulus, G'' is the loss modulus, η' is the real part of the complex viscosity, and η'' is the imaginary part of the complex viscosity with $\eta^* = \eta' - i\eta''$ defined as the complex viscosity. The magnitude of the complex viscosity is given by $|\eta^*| = \sqrt{\eta'^2 + \eta''^2}$. η' and η'' can be calculated from the shear-rate averaged, or strain

averaged shear stresses as[37 and 40]

$$\eta' = \frac{\int_0^{2\pi/\omega} \sigma(t) \cos(\omega t) dt}{\dot{\gamma}_0 \int_0^{2\pi/\omega} \cos^2(\omega t) dt} = \frac{\int_0^{2\pi/\omega} \sigma(t) \dot{\gamma}(t) dt}{\int_0^{2\pi/\omega} \dot{\gamma}(t)^2 dt} = G''/\omega, \quad (7)$$

$$\eta'' = \frac{\int_0^{2\pi/\omega} \sigma(t) \sin(\omega t) dt}{\dot{\gamma}_0 \int_0^{2\pi/\omega} \sin^2(\omega t) dt} = \frac{\int_0^{2\pi/\omega} \sigma(t) \gamma(t) dt}{\int_0^{2\pi/\omega} \gamma(t)^2 dt} = G'/\omega. \quad (8)$$

Note that these quantities can always be calculated and defined even if one is not in a linear regime. Following our previous approach[37], we generalise Eqs. 7 and 8, applying it also to pressures/normal stresses (see the SI) and stress ratios

$$\mu' = \frac{\int_0^{2\pi/\omega} (\sigma/P) \dot{\gamma}(t) dt}{\int_0^{2\pi/\omega} |\dot{\gamma}(t)| dt}, \quad (9)$$

$$\mu'' = \frac{\int_0^{2\pi/\omega} (\sigma/P) \gamma(t) dt}{\int_0^{2\pi/\omega} |\gamma(t)| dt}, \quad (10)$$

where μ' is the viscous component, μ'' is the elastic component of the complex macroscopic friction coefficient μ^* , with the magnitude equal to $|\mu^*| = \sqrt{\mu'^2 + \mu''^2}$.

A shear-rate averaged viscous number J' is defined in the same way as in [37],

$$J' = \frac{\eta_f \int_0^{2\pi/\omega} (\dot{\gamma}/P) \dot{\gamma} dt}{\int_0^{2\pi/\omega} |\dot{\gamma}| dt}. \quad (11)$$

One can equivalent define J'' , but can easily be seen to be equal to zero due to the $\dot{\gamma}\gamma$ -term. Other properties such as the packing fraction ϕ and the number of contacts Z are generally less sensitive to the averaging process, being that the shear-rate-weighted-average, the strain-weighted-average, or the direct time-average (see the SI for a comparison). We, therefore, calculate the average of ϕ and Z as

$$A = \frac{\int_0^{2\pi/\omega} A(t) (|\dot{\gamma}(t)| + |\omega\gamma(t)|) dt}{\int_0^{2\pi/\omega} (|\dot{\gamma}(t)| + |\omega\gamma(t)|) dt}, \quad (12)$$

where A is either ϕ or Z . As $\int_0^{2\pi/\omega} (|\dot{\gamma}(t)| + |\omega\gamma(t)|) dt = 2$, this is in principal the arithmetic mean between the strain and shear-rate averaged quantities.

IV. RESULTS AND DISCUSSIONS

A. VISCOELASTIC RESPONSE

1. Time series and Lissajous curves

In Fig. 1, we show some examples of time series of the rescaled stress $\sigma/|\eta^*|\dot{\gamma}_0$ compared to the rescaled

shear-rate $\dot{\gamma}/\dot{\gamma}_0$ and the strain γ/γ_0 at $J' \simeq 3 \cdot 10^{-3}$ for suspensions composed of (a) frictional or (b) frictionless particles at three different strain magnitudes. The black lines in the sub-figures are all analytical predictions of how the stress will respond if its corresponding steady-shear rheology could describe the suspensions at each given time (*i.e.* corresponding to an instantaneous relaxation of the microstructure and stresses upon changes in shear-rate). The analytical predictions are given by $\sigma = \mu(J)P$ and $\mu(J) = \mu_c + a_\mu J^{n_\mu}$, where $\mu_c = 0.28$, $a_\mu = 2.5$, $n_\mu = 0.5$ for the frictional case and $\mu_c = 0.09$, $a_\mu = 1.3$, $n_\mu = 0.38$ for the frictionless case [37 and 41]. In these predictions, we have accounted for that ϕ varies with a varying $\dot{\gamma}$ at constant pressure or equivalent to an instantaneous J . The average packing fractions of the dense suspensions at oscillatory shear flows are generally found to increase as γ_0 decreases (see SI). For the specific cases in Fig. 1 we find the couples $[\gamma_0, \phi]$: $[10, 0.764]$, $[0.33, 0.800]$, and $[0.0033, 0.835]$ in (a) and $[10, 0.817]$, $[0.33, 0.823]$, and $[0.0033, 0.839]$ in (b).

For $\gamma_0 = 10$ the stress curves, both for the frictional and frictionless case, follow our analytic predictions with an excellent agreement (see Fig. 1), illustrating that at large strain rates, the oscillatory rheology can be indeed inferred from the steady shear one (*i.e.*, respecting the Cox-Merz rule). At first sight, the stress response seems non-linear (*i.e.*, not being a simple linear combination of the strain and strain-rate curves), which could be considered as being in the non-linear LAOS-regime. However, we find here that the simulation results well-follow our analytical prediction, which is a clear sign that at $\gamma_0 = 10$ the suspension behaves as if under steady shear at each given time. The seemingly non-linearity in the stress response is instead caused by the varying packing fraction in our pressure controlled set-up (see the SI for the corresponding time-series of ϕ) and is well captured by our analytical prediction. Both experimental and numerical shear reversal results at constant volume [27 and 29] have shown that one recovers the steady-shear microstructure after a shear-reversal and a finite strain, with the viscosity saturating to the steady-shear value. Our results for large strain amplitudes imply that the same occurs under constant pressure. It should be further noted that our steady-state predictions only include viscous responses (or equivalent loss moduli) in the description of the stresses; hence an agreement with analytic predictions implies a pure (linear) viscous response. In real systems, one usually finds non-linearities at large amplitudes, *i.e.* large shear-rates, due to, *e.g.*, inertial effects and/or particle deformations. These effects have not been considered in the current model, and, hence, the Cox-Merz rules arises naturally from the linearity of the system. As γ_0 decreases, the stress curves, in both cases (frictional and frictionless), start to deviate from the analytical predictions, implying a viscoelastic response.

An alternative way to represent and illustrate the viscoelastic response is by Lissajous curves. In Fig. 2 and 3, we show Lissajous curves for suspensions composed of frictional or frictionless particles respectively at various strain magnitudes as indicated by the legend. The Lissajous curves show the rescaled shear stresses as functions of (a) shear-rate $\dot{\gamma}/\dot{\gamma}_0$ and (b) strain γ/γ_0 . The arrows indicate the directions of the curves. As before, the black dashed lines are analytical predictions assuming that the stress responses are linear, viscous, instantaneous, and described by their corresponding steady-shear rheology. Comparing Fig. 2 with 3, we do not see much difference in the Lissajous curves between frictional and frictionless suspensions at the same γ_0 . In both cases, the Lissajous curves with $\gamma_0 = 10$ are in good agreement with the analytical predictions, indicating that the behaviours of the suspensions still follow steady-shear rheology at large strain magnitudes and hence respect the Cox-Merz rule even at pressure imposed conditions. As γ_0 decreases, the Lissajous curves deviate from the steady-shear predictions. At $\gamma_0 < 0.1$, which is usually associated with the SAOS-regime, one would expect to see ellipses in the Lissajous curve, being an indicator of linear viscoelastic response. In the cases here, however, we observe twisted ellipses. It is hard to say if such a shape is evidence of a non-linear response or a result of a varying packing fraction (still with linear viscoelasticity). or a result from a varying packing fraction (still with linear viscoelasticity).

In general, it is hard to directly map our results into the framework of SAOS and LAOS due to the pressure imposed set-ups we use here. To do so, one needs to know how packing fractions vary and their consequences for both the viscous and elastic response. Currently, we lack information about the latter response. In the following, we will try to circumvent this difficulty by looking at the complex, real, and imaginary viscosities and our generalisation of a complex macroscopic friction coefficient.

2. Total response

Fig. 4 shows complex viscosities as functions of packing fraction for the suspensions composed of (a) frictional and (b) frictionless particles. At large strain magnitudes $\gamma_0 = 10$ and $\gamma_0 = 3.3$, the viscosities have the same packing fraction dependencies as in their corresponding steady-shear cases [41] (indicated by black symbols and lines). Above shows, together with the time-series of the stresses, that steady-state can be used to understand the oscillatory rheology at large oscillatory strains and vice versa, *i.e.*, that the Cox-Merz rule is applicable in these linear models. As γ_0 becomes smaller, the complex viscosities start to deviate from the steady-shear cases, as seen previously for the time-series and Lissajous plots

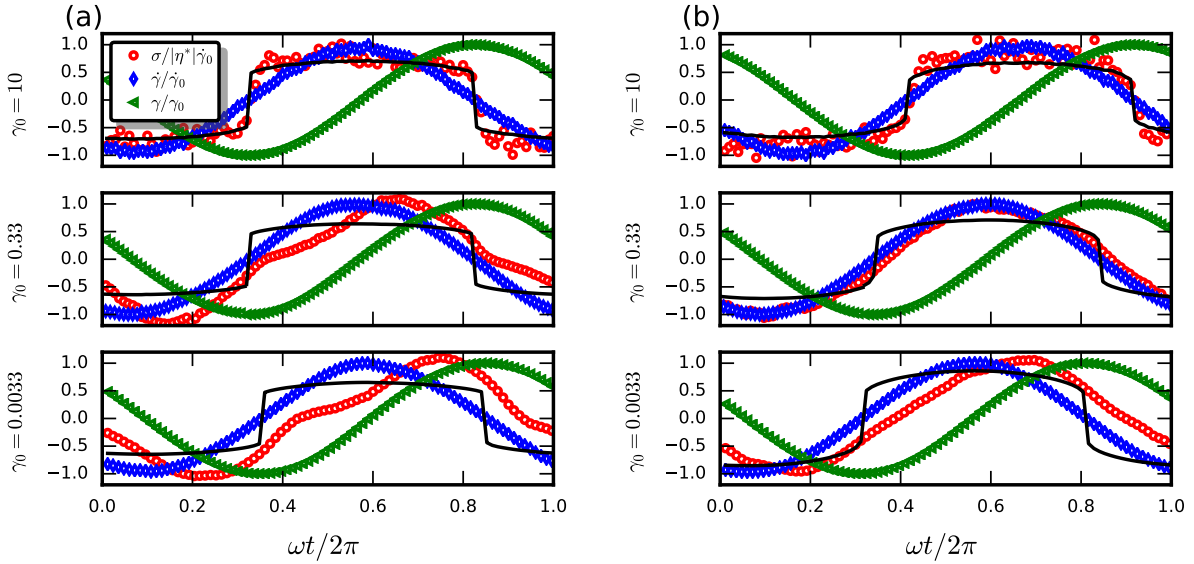


FIG. 1. Time series of rescaled shear stress $\sigma/|\eta^*|\dot{\gamma}_0$ (red circles) where $|\eta^*|$ is the magnitude of complex viscosity for the corresponding case, shear-rate $\dot{\gamma}/\dot{\gamma}_0$ (blue diamonds), strain γ/γ_0 (green triangles) for (a) frictional suspensions ($\mu_p = 0.4$) and (b) frictionless suspensions ($\mu_p = 0$) at $J' \simeq 3 \cdot 10^{-3}$ and three different γ_0 (10, 0.33, and 0.0033) as indicated in the labels to the left of the figures. The values of $|\eta^*|/\eta_f$ are 139 ($\gamma_0 = 10$), 194 ($\gamma_0 = 0.33$), and 180 ($\gamma_0 = 0.0033$) in (a), and 99 ($\gamma_0 = 10$), 96 ($\gamma_0 = 0.33$), and 76 ($\gamma_0 = 0.0033$) in (b). The black lines are analytical prediction corresponding to a purely viscous stress response.

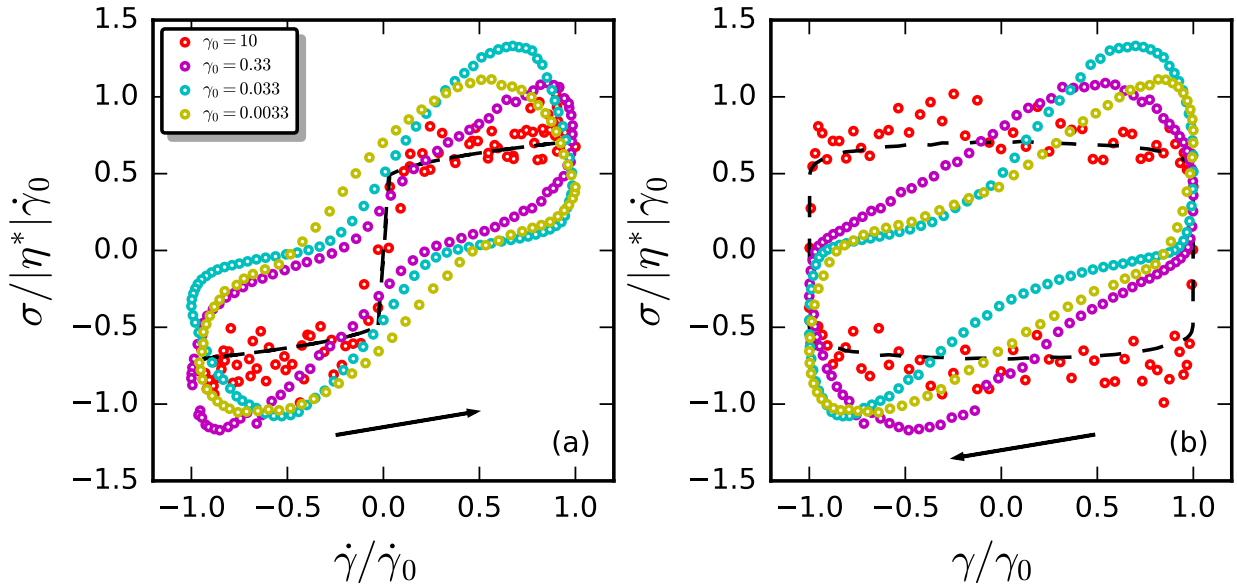


FIG. 2. Lissajous curves of stress for frictional suspensions ($\mu_p = 0.4$) at $J' \simeq 3 \cdot 10^{-3}$ and various strain magnitude γ_0 as indicated in the legends, as functions of (a) shear-rate $\dot{\gamma}/\dot{\gamma}_0$ and (b) strain γ/γ_0 . The shear stresses σ are normalised as in Fig. 1, with $|\eta^*|/\eta_f$ -values equal to 139 ($\gamma_0 = 10$), 194 ($\gamma_0 = 0.33$), 238 ($\gamma_0 = 0.033$) and 180 ($\gamma_0 = 0.0033$). The black dashed lines are plots of the analytical predictions, and the arrows indicate the directions.

of the corresponding cases, with a reduced complex viscosity as the strain amplitude is lowered. These trends correlate well with what we previously found when only considering the real part of the viscosity [37]. The main difference between the frictional and the

frictionless cases is that the jamming packing fraction ϕ_c for the frictional suspensions is shifted to a higher value at small strain magnitudes ($\gamma_0 \leq 0.1$). In contrast, for the frictionless suspensions ϕ_c does not show such apparent shift [35 and 37]. The effect of varying γ_0 on

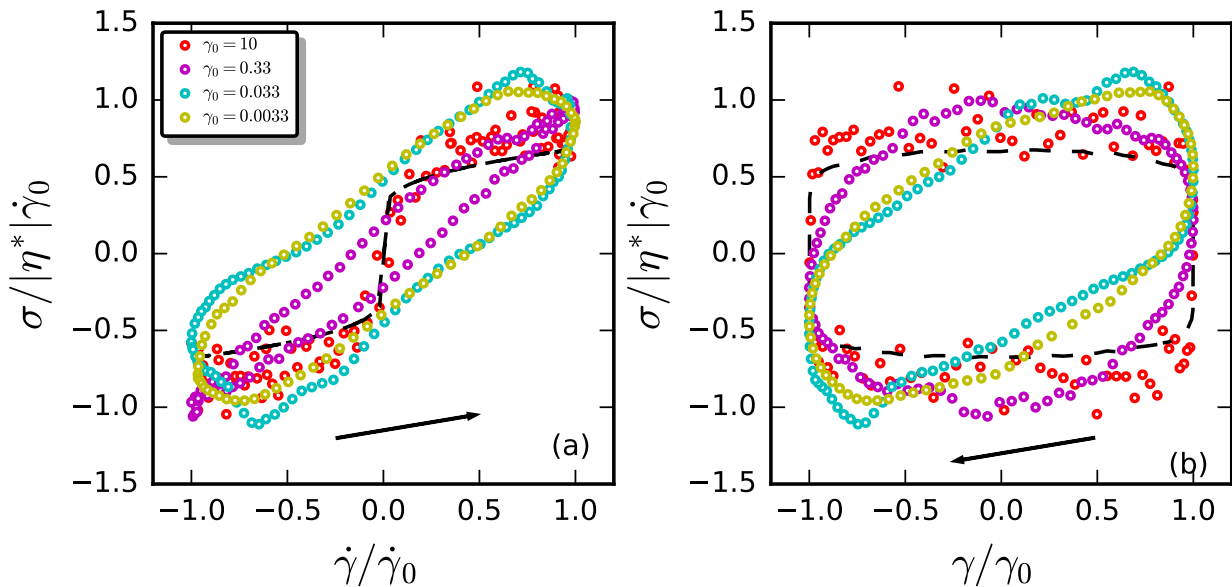


FIG. 3. As in Fig.2 but for frictionless suspensions ($\mu_p = 0$). The values of $|\eta^*|/\eta_f$ are 99 ($\gamma_0 = 10$), 96 ($\gamma_0 = 0.33$), 97 ($\gamma_0 = 0.033$) and 76 ($\gamma_0 = 0.0033$).

ϕ_c is better illustrated when studying ϕ as functions of shear-rate averaged viscous number J' , see Fig. 5. For fixed γ_0 values, all curves show a monotonically increasing packing fraction as J' is decreased. Similar as in Fig. 4, we see that both $\gamma_0 = 10$ and 3.3 curves collapse on top of the steady-shear curve. As γ_0 is decreased, the packing fractions do, however, increase at large J' values. As J' approaches zero (and hence shear jamming with its corresponding critical packing fraction ϕ_c) one sees a clear and almost discontinuous jump in the packing fraction curves when lowering the strain amplitude below $\gamma_0 < 0.33$ for the frictional case. For $\gamma_0 > 0.1$ and frictional particles, ϕ_c coincides with the same value as found in steady state, denoted by $\phi_c^{f,SS}$, while for $\gamma_0 < 0.33$ ϕ_c is closer but still below the critical packing fraction found for frictionless particles in steady shear, denoted by $\phi_c^{nf,SS}$. The inset of Fig. 5(a) shows a zoom-in close to shear jamming. For frictionless cases, a shift in ϕ_c is less apparent (see the inset of Fig. 5(b)). However, for the lowest studied J' -values we see a non-monotonic dependency of the packing fractions as a function of γ_0 and with the maximum packing fraction occurring at around $\gamma_0 = 0.1$ (see Fig. 6(b) for values of ϕ at $J' \simeq 4 \cdot 10^{-4}$, one of our lowest J' values). Nevertheless, all curves seem to have a packing fraction approximately equal or less to the critical packing fraction $\phi_c^{nf,SS}$ for frictionless particles at steady shear. It should, however, be noted that the value of $\phi_c^{nf,SS}$ vary slightly ($\phi_c^{nf,SS} \in [0.845, 0.848]$) depending on the range of J' used when estimating it, this uncertainty is indicated by a shaded region in the inset of Fig. 5(b). Some of the packing fractions in the low J' limit and at low γ_0 are all within this shaded area; hence we can not tell by certain if there is a shift or not in ϕ_c . We

continue by estimating the ϕ_c values at different γ_0 for suspensions composed of either frictional or frictionless particles by fitting the data in the low J' -limit (typically $J' < 10^{-2}$) to $\phi = \phi_c + a_\phi (J')^{n_\phi}$, where ϕ_c , a_ϕ and n_ϕ are all free parameters. Fig. 5(c) shows how the ϕ_c values vary as a function of γ_0 . For frictionless particles, we find ϕ_c to be the same or below $\phi_c^{nf,SS}$. However, our standard error of the estimates are all on the order of the shifts; hence we currently lack the precision to actually conclude. For frictional particles, there is, however, a clear and seemingly discontinuous transition in the values of ϕ_c as γ_0 varies, from the values around $\phi_c^{f,SS}$ at large strains to values around $\phi_c \sim 0.835 < \phi_c^{nf,SS}$ as γ_0 drops below 0.33. To further investigate the nature of this transition in ϕ_c for the frictional particles, we run a few simulations at $J' \simeq 4 \cdot 10^{-4}$ (*i.e.* close to shear jamming) and $\gamma_0 \in [0.033, 0.33]$. The results are presented in Fig. 6(a), where we find a gradual increase in ϕ as γ_0 decreases, indicating that the transition of ϕ_c for the frictional suspensions is actually continuous in a narrow γ_0 range, starting at $\gamma_0 = 0.3$ and fully completed at $\gamma_0 = 0.05$.

Fig. 7 shows how the complex friction coefficient $|\mu^*|$ varies as a function of J' at various γ_0 for (a) frictional and (b) frictionless particles. In general, $|\mu^*|$ shows a similar trend as seen in steady shear, namely $|\mu^*|$ increases with J' from a finite value $|\mu^*|_c$ at $J' = 0$ (represented by the plateau at low J' values in the lin-log representation). At $\gamma_0 = 10, 3.3$ and 1, $|\mu^*|$ behaves approximately the same as for the steady-shear cases. At smaller γ_0 , the $|\mu^*|$ values in the low J' -branch are all consistently lower than the corresponding steady-shear values. For larger J' values, we could not see any clear

trend (alternating between being both larger or smaller compared to the corresponding steady shear value as γ_0 is varied). Values of $|\mu^*|_c$ (*i.e.* $|\mu^*|$ as $J' \rightarrow 0$) were extracted in the same way as was done for ϕ_c , *i.e.* but fitting the data to $|\mu^*| = |\mu^*|_c + a_\mu (J')^{n_\mu}$ in the low J' -branch (typically $J' < 10^{-2}$). The results are plotted as a function of γ_0 in Fig. 7(c), where transitions can be seen for both the frictional and frictionless particles, from values equal to the steady-shear ones at large γ_0 to smaller values as γ_0 decreases. The transition can be described by a phenomenological hyperbolic function $|\mu^*|_c = \mu_c^{\text{SS}} [1 - k_1 \tanh(k_2/\gamma_0)]$, where μ_c^{SS} is the value of μ_c for the suspension at steady shear and k_1 and k_2 are two free parameters. k_2 signals at around which γ_0 -value the transition occurs. For frictional particles we found $k_2 = 0.04 \pm 0.01$ and for frictionless particles $k_2 = 0.005 \pm 0.003$. k_1 instead signals the maximal decrease in $|\mu^*|_c$ due to oscillations, where $\mu_c^{\text{SS}}(1 - k_1)$ gives the value of $|\mu^*|_c$ as $\gamma_0 \rightarrow 0$. For frictional particles we found $k_1 = 0.29 \pm 0.03$ and for frictionless particles $k_1 = 0.88 \pm 0.25$, *i.e.*, a 30% and 80-100% decrease in $|\mu^*|_c$ respectively as $\gamma_0 \rightarrow 0$.

3. Decomposition of the complex viscosity and macroscopic friction

One of the most common measurement in characterising viscoelastic materials are the storage modulus G' and loss modulus G'' , or equivalently the viscous (real) component of complex viscosity η' and the elastic (imaginary) component η'' . In this section, we present results of η' and η'' , as well as μ' and μ'' , previously defined in section *Suspensions Rheology*. In Fig. 8 and 9, we show how μ' and μ'' vary with J' for suspensions composed of frictional and frictionless particles respectively. The $\mu'(J')$ -rheology are in both cases similar in behaviour to the steady shear curve. The main difference is that the curves shift to lower values compared to steady-state as γ_0 decreases. Fig. 10(a) shows μ'_c as a function of γ_0 where we see a similar behaviour as for $|\mu^*|_c$ with slightly lower values in the low γ_0 -branch.

The elastic component μ'' is, on the other hand, the smallest, for a given J' value, at large γ_0 values (see Fig. 8(b)). Several of the μ'' -curves show a non-monotonic trend as a function of J' . The location of the minimum seems to vary with γ_0 , leading to a non-monotonicity also in μ''_c as a function of γ_0 for a fixed J' , as seen in Fig. 10(b) where we have estimated μ''_c to be equal to the value of μ'' at our lowest J' studied values. For the largest γ_0 the elastic component is close to zero, in agreement with what one would expect for a suspension with steady-shear rheology (*i.e.* an almost pure viscous response).

Fig. 11 shows the relative importance of the viscous/elastic components to the overall complex quantities ($\mu'^2/|\mu^*|^2 = 1 - \mu''^2/|\mu^*|^2$, $\eta'^2/|\eta^*|^2 = 1 - \eta''^2/|\eta^*|^2$) as functions of J'/γ_0 for the suspensions composed of fric-

tional particles. At large strain magnitudes ($\gamma_0 \geq 1$), we have almost a pure viscous response. As γ_0 decreases, the elastic response becomes increasingly important. This is agreement with previous LAOS results of yielded dense Brownian suspensions in the high Péclet-regime[25]. By normalising the viscous number J' by γ_0 , we obtain a decent collapse of the data for $\eta'^2/|\eta^*|^2$ and $\gamma_0 \leq 0.1$, as seen in Fig. 11(b). We do not observe the same collapse, however, for $\mu'^2/|\mu^*|^2$ (see Fig. 11(a)), instead we see that the peak values (if any) are γ_0 -dependent. At small J'/γ_0 values, one sees a difference in the rheological behaviour depending on the value of γ_0 . As $\gamma_0 > 0.1$ we see that the behaviour dominantly viscous as we approach its corresponding shear jamming point ($J'/\gamma_0 \rightarrow 0$). At $\gamma_0 < 0.33$, the opposite is true; its elastic response dominates the shear-jamming. This transition correlates well with a change in the shear-jamming packing fraction for the frictional case. We do not attribute the emergence of elastic response to the elasticity of the particles as increasing the spring constants lead to the same curve (see the SI). Instead, we interpret this emergence of elasticity as coming from a not fully developed restructuring of the microstructure upon shear-reversal. A restructuring upon shear-reversal takes, in general, a finite and small strain, typically of the order of one, to be completed [27–29].

Surprisingly, frictionless suspensions show a similar change in their rheological behaviour, see Fig. 12, even though there is no clear shift in ϕ_c for these cases. Hence, while there might be a correlation between the shift in ϕ_c and the transition from viscous to viscoelastic or even an elastic response as γ_0 decreases, there is no clear causality between these two observations. Comparing Fig. 12 to Fig. 11, we see a similar behavior of both the frictional and frictionless cases, with slightly worse collapsed of $\eta'^2/|\eta^*|^2$ as a function of J'/γ_0 for the low γ_0 values.

4. Effect of lubrication forces and fluid stresses

So far, we have neglected both contributions from lubrication forces and the fluid stress itself to the overall shear stress. The latter can be quite simply be corrected by adding a term η_f to the loss modulus. This will mostly affect the curves where the complex viscosity (without the fluid stress) is small; see, *e.g.*, Fig. 4 above and Fig. 1 in the SI. As a first approximation, one could argue that the lubrication forces acts as a mean-field viscosity with increased *effective* fluid viscosity, η_f^{eff} , as a result. Assuming that this *effective* viscosity has a moderate dependence on the packing fraction, one could rationalise this effect by a redefinition of J' as well as a simple upscaling of the stresses $\sigma \propto \eta_f^{\text{eff}}$ rather than $\sigma \propto \eta_f$. However, as the packing fraction is increased, the stresses become dominated by the contact stresses, and our approximation of neglecting stresses from lubrication forces and the fluid itself becomes increasingly accurate. That the viscoelastic response is predominantly

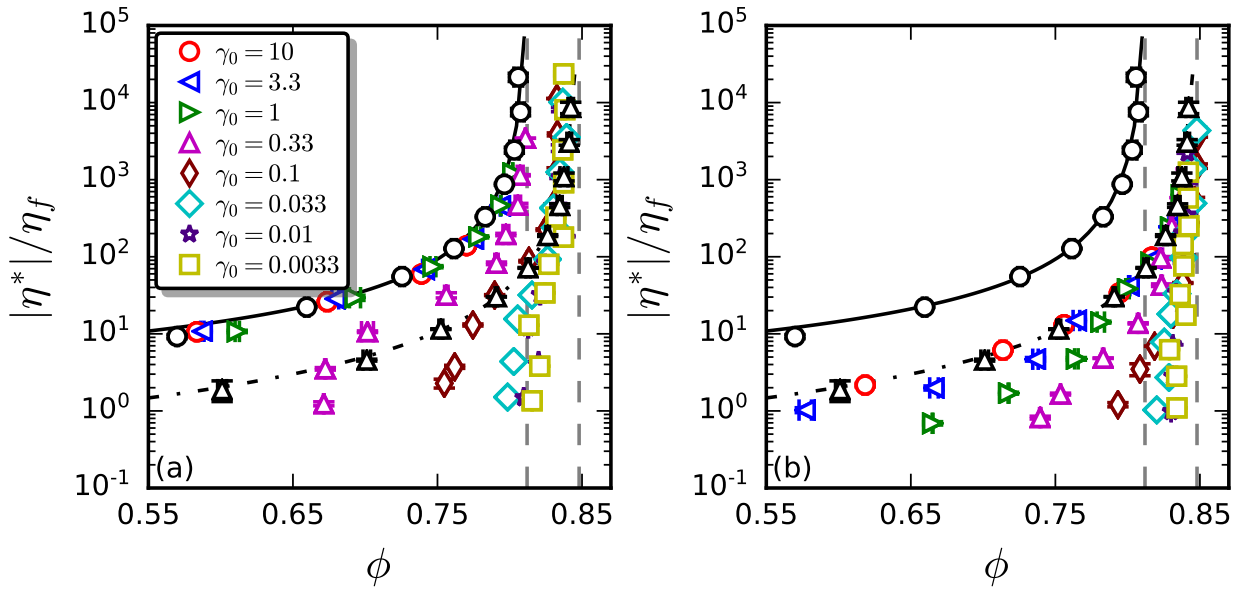


FIG. 4. Rescaled complex viscosities $|\eta^*|/\eta_f$ as a function of the packing fraction ϕ at various strain magnitude γ_0 as indicated in the legends for the suspensions composed of (a) frictional ($\mu_p = 0.4$) and (b) frictionless ($\mu_p = 0$) particles. The black circles and black triangles are viscosities under steady shear for frictional and frictionless cases, respectively. The black lines are constitutive laws for suspensions under steady shear. The constitutive laws are given as $\eta/\eta_f = a(\phi - \phi_c)^{-n} + a'(\phi - \phi_c)^{1-n}$, where $a = 0.18$, $n = 2$, $a' = 1.9$ for the frictional case and $a = 0.004$, $n = 2.7$, $a' = 0.18$ for the frictionless case[41]. ϕ_c is the shear jamming packing fraction for suspensions under steady shear as indicated by the grey vertical lines with $\phi_c^f = 0.812 \pm 0.002$ for frictional and $\phi_c^{nf} = 0.848 \pm 0.002$ for frictionless cases.

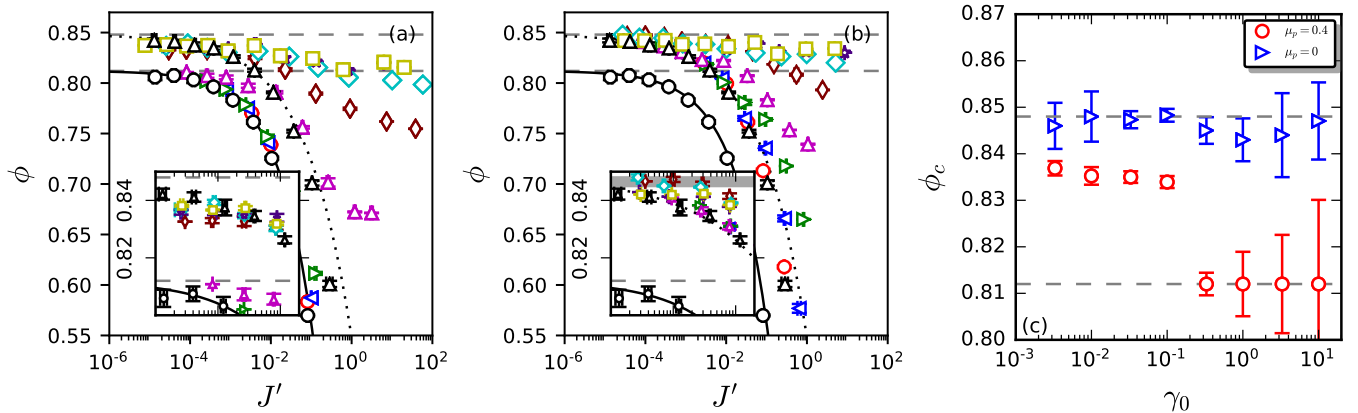


FIG. 5. Packing fraction ϕ as a function of the viscous number J' at various γ_0 for (a) frictional and (b) frictionless suspensions. The colours and symbols are the same as in Fig. 4. The black symbols correspond to the steady-shear conditions, and the black lines are plots of the constitutive laws for the steady-shear cases. The constitutive laws are $\phi = \phi_c - a_\phi J'^{n_\phi}$, where $a_\phi = 0.79$, $n_\phi = 0.5$ for the frictional case and $a_\phi = 0.3$, $n_\phi = 0.38$ for the frictionless case[41]. The grey dashed horizontal lines indicate the values of ϕ_c for suspensions under steady shear (the values of ϕ_c are given in the caption of Fig. 4). The insets are zoomed-in figures of the main figures close to jamming. In (c) jamming packing fraction ϕ_c as a function of γ_0 for both the frictional and frictionless suspensions, the grey dashed horizontal lines are again indications of the steady-shear values of ϕ_c .

caused by the contact stresses can be, for example, seen in the work by Ness, Xing, and Eiser [31] (see their Fig. 3). For completeness, we provide additional data in the SI, where lubrication forces have been accounted for. As stated above, this mostly affects the low packing fraction region (equivalent to the high J' -regime) and does not change any of our conclusions regarding what happens

when approaching the shear-jamming regime.

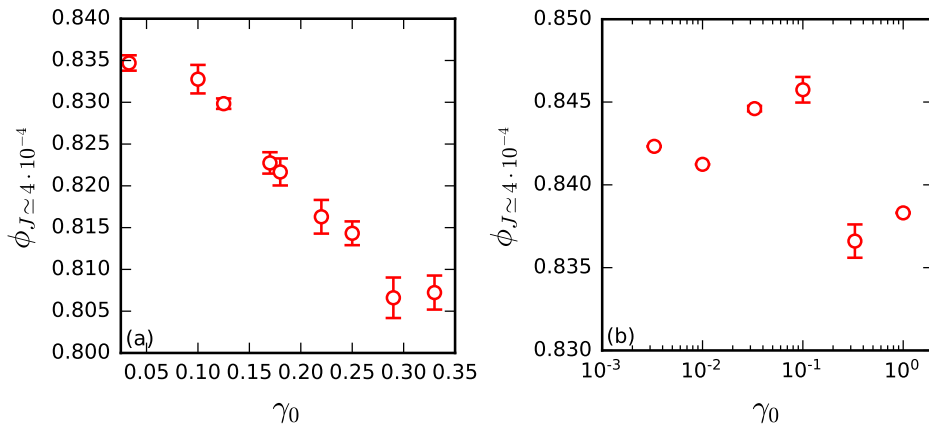


FIG. 6. Packing fraction ϕ as a function of the strain magnitude γ_0 at $J' \simeq 4 \cdot 10^{-4}$ for suspensions composed of (a) frictional particles and (b) frictionless particles.

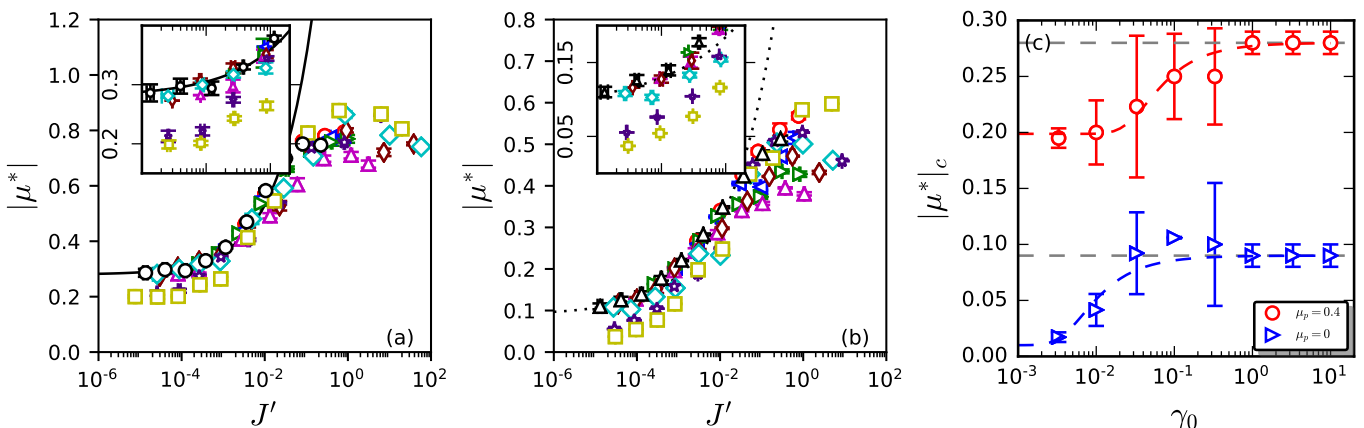


FIG. 7. Complex macroscopic friction $|\mu^*|$ as a function of the viscous number J' at various γ_0 for (a) frictional and (b) frictionless suspensions. The colours and symbols follow the same styles as in Fig. 4, with zoomed-in figures close to $J' \rightarrow 0$ as insets. The black symbols are data for the suspensions under steady shear, and the black lines are plots of the constitutive laws for the steady-shear cases. The constitutive laws are $\mu = \mu_c + a_\mu J'^{n_\mu}$. The values of the parameters have been given in section IV.A.1[41]. In (c) $|\mu^*|_c$ as a function of γ_0 ; the coloured dashed lines are best fits of the phenomenological function $|\mu^*|_c = \mu_c^{\text{SS}} [1 - k_1 \tanh(k_2/\gamma_0)]$, where μ_c^{SS} is the values of suspensions under steady shear with $\mu_c^{\text{f,SS}} = 0.28$ for the frictional suspensions and $\mu_c^{\text{nf,SS}} = 0.09$ for the frictionless suspensions; k_1 and k_2 are two fitted parameters, the values are given in text. The grey dashed horizontal lines indicate the values of the corresponding μ_c^{SS} .

B. MICROSCOPIC STRUCTURE

1. Number of contacts

Fig. 13 shows how the number of contacts per particle Z evolves as J' varies for a suspension composed of (a) frictional or (b) frictionless particles at different γ_0 . In general, we find that Z follows the same curves as for steady-state. The exception is again at small $\gamma_0 (\leq 1)$, where we get smaller Z values compared to steady-state's Z_c^{SS} . This exception can be better seen in the insets of the figure. As before, we estimate the values of Z_c at different γ_0 by fitting the data to $Z = Z_c - a_Z (J')^{n_Z}$ with $J' < 10^{-2}$, where Z_c , a_Z and n_Z are three free fitting parameters. The results are presented in Fig. 13(c) as functions of strain magnitude γ_0 ,

where we find a similar behaviour as for the complex macroscopic friction coefficients (see Fig. 7(c)). We again fit the data to a phenomenological hyperbolic function $Z_c = Z_c^{\text{SS}} [1 - c_1 \tanh(c_2/\gamma_0)]$, where Z_c^{SS} is the value of Z_c for steady-shear and equal to 3.18 for the frictional particles and 3.93 for the frictionless case; c_2 shows at around which γ_0 -value one sees a shift in the number of contacts per particle (at shear-jamming). For the frictional case we find $c_2 = 0.53 \pm 0.21$ and for the frictionless case $c_2 = 0.23 \pm 0.05$. Interestingly these shifts occur at considerably larger γ_0 values than we have seen previously for $|\mu^*|$; hence there is no direct link between these two quantities. Instead, the change is better correlated with the change in ϕ_c (if any). $Z_c^{\text{SS}} (1 - c_1)$ gives the Z_c value as $\gamma_0 \rightarrow 0$, where we find $c_1 = 0.08 \pm 0.007$ (frictional) and $c_1 = 0.04 \pm 0.002$ (frictionless) leading to

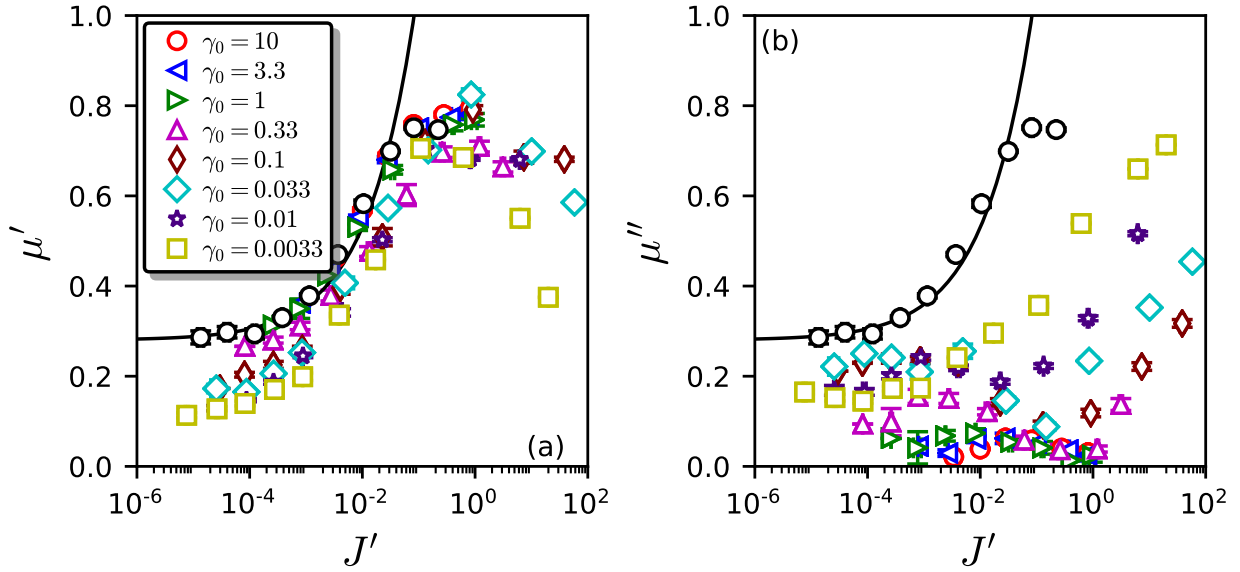


FIG. 8. (a) μ' and (b) μ'' as a function of J' for the frictional suspensions at different γ_0 as indicated by the legends; the black circles are the values of μ for the frictional suspensions under steady shear, and the black lines are plots of the constitutive laws for the steady-shear case. The constitutive laws are the same as in Fig. 7(a).

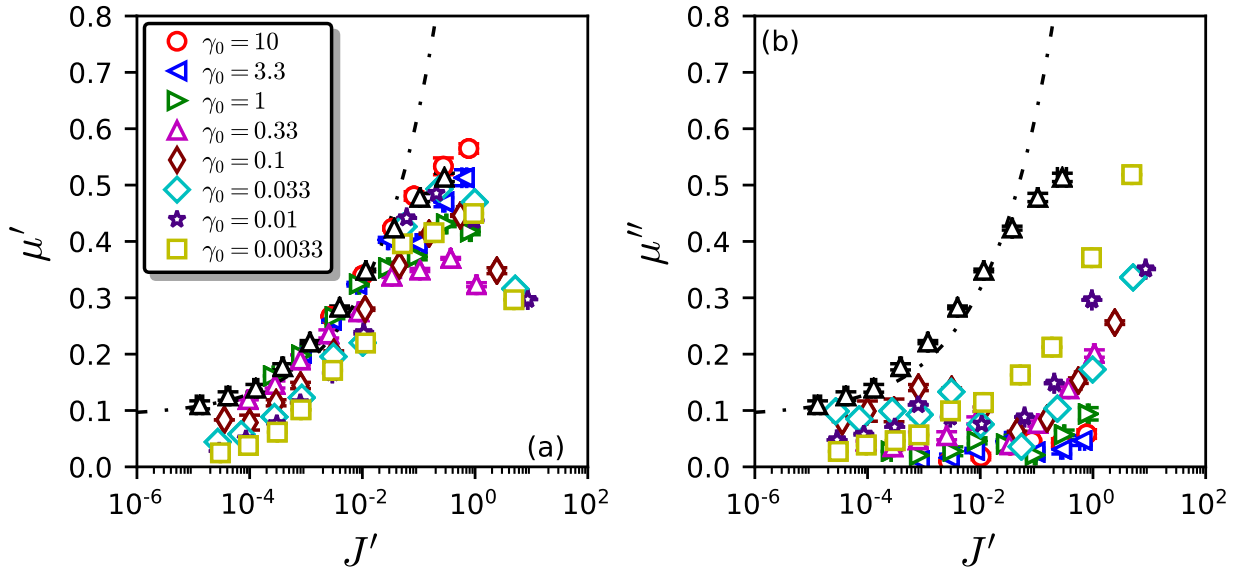


FIG. 9. As in Fig. 8 but for frictionless particles, the constitutive laws are the same as in Fig. 7(b).

$Z_c = 2.96$ (frictional) and $Z_c = 3.77$ (frictionless) for small γ_0 -values. These values show that the frictional case is isostatic (*i.e.*, very close to 3) while the frictionless is hypostatic (*i.e.*, considerable less than 4). Rattlers have, however, not been excluded in these estimates. Excluding rattlers would increase the number of contacts (per no rattling particle) slightly.

Frictional particles at contact can either undergo sliding or rolling motions. For $\mu_p = 0.4$, the frictional sliding dominates the energy dissipation close to shear

jamming[42]. In addition, the frictional sliding contributes to a higher shear jamming packing fraction than for suspensions composed of frictional particles without sliding[43 and 44]. This could explain why we see an increased packing fraction in the frictional case but not the frictionless (where all contacts can be regarded as sliding), as oscillations could alter the fraction of sliding particles. Fig. 14(a) shows the number of sliding contacts per particle Z_s as a function of J' at various γ_0 . At $\gamma_0 \geq 0.33$, the curves are again overlapping with the steady-shear one. As γ_0 is lowered, one can see a decrease

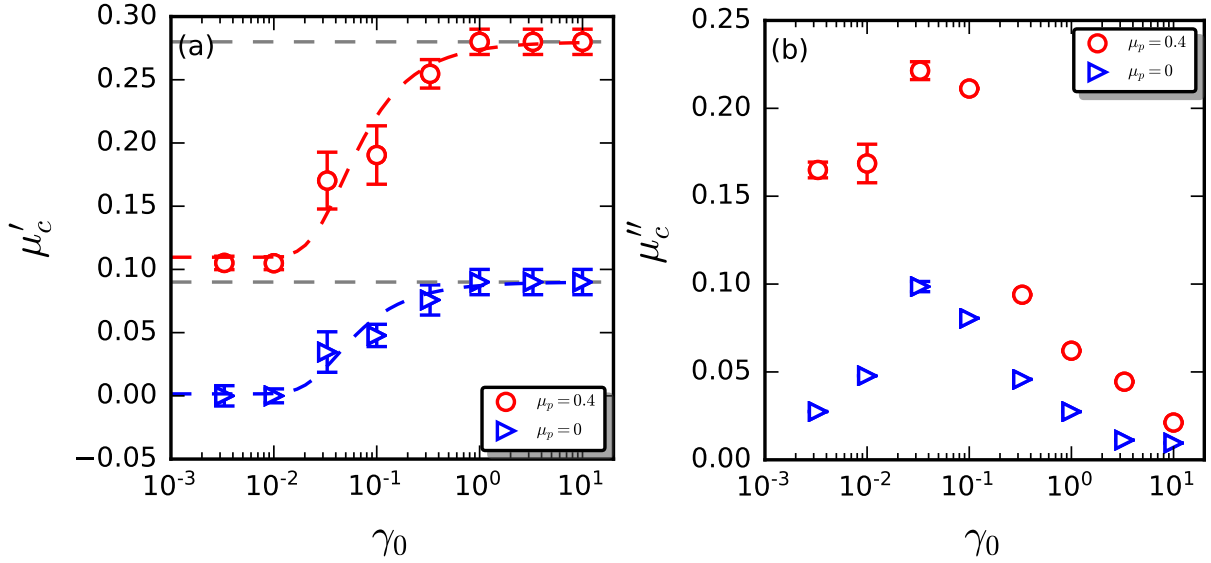


FIG. 10. (a) μ'_c and (b) μ''_c as a function of γ_0 for suspensions composed of frictional or frictionless particles. Dashed grey horizontal lines in (a) show the corresponding values in steady shear.

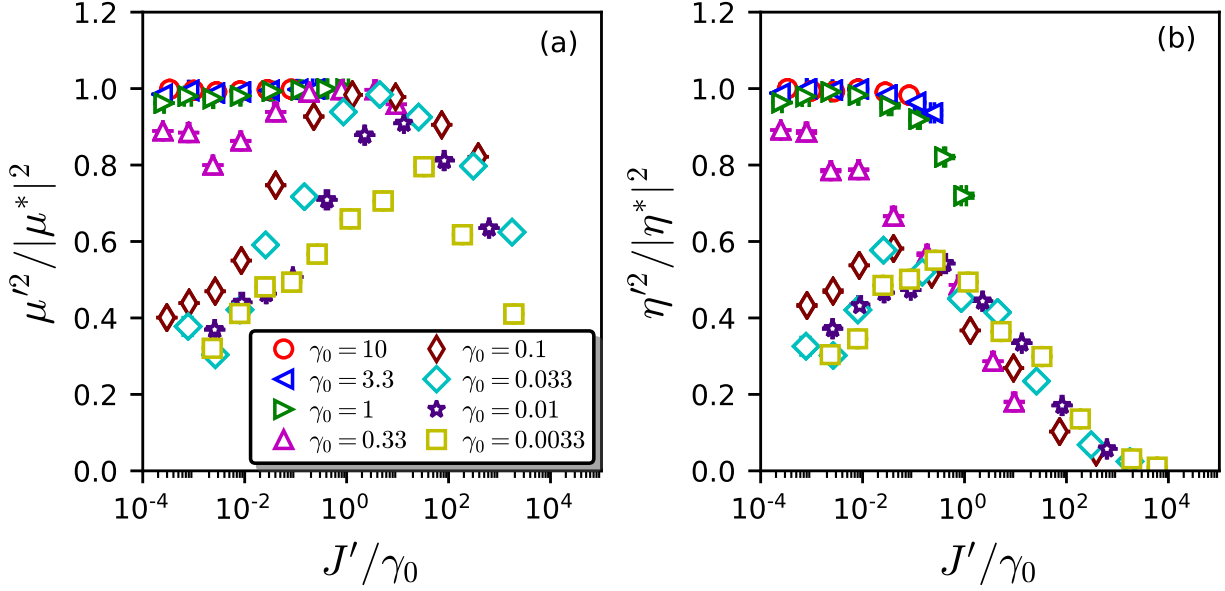


FIG. 11. (a) $\mu'^2/|\mu^*|^2$ and (b) $\eta'^2/|\eta^*|^2$ as a function of J'/γ_0 for the suspensions composed of frictional particles at various γ_0 as indicated by the legend.

in Z_s and the fraction of sliding contacts $\chi_s = Z_s/Z$; see Fig. 14(b). A lower fraction of sliding contacts would indicate a smaller packing fraction in general, in contradiction to what is found (see Fig. 5). Hence, the increased packing fractions are not explained by a decrease in the number of sliding contacts per particle or fraction of them but rather by reducing the overall number of contacts.

2. Geometrical contact fabric

The geometrical contact fabric gives the probability of having a contact at a certain angle, where the angle is between the vector, which connects the particles at contact and the axis parallel to the walls[45]. The shear-rate averaged geometrical contact fabric is calculated, in a similar way as for the other shear-rate averaged quantities, as

$$\xi(\theta) = \frac{\int_0^{2\pi/\omega} \xi(\theta, t) |\dot{\gamma}(t)| dt}{\int_0^{2\pi/\omega} |\dot{\gamma}(t)| dt}. \quad (13)$$

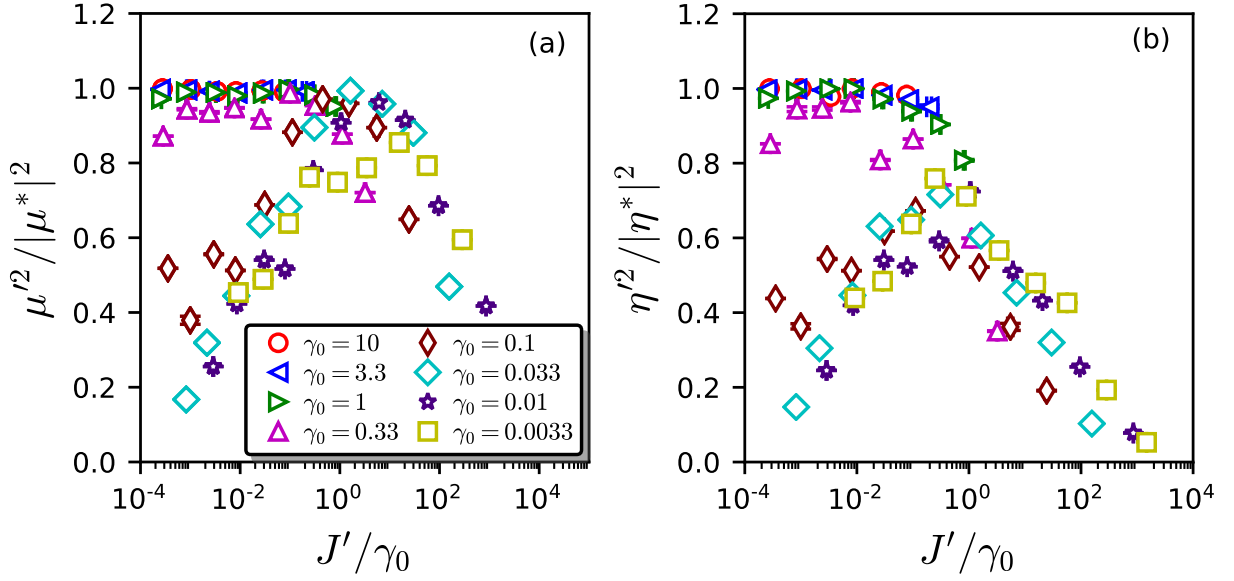


FIG. 12. (a) $\mu'^2/|\mu^*|^2$ and (b) $\eta'^2/|\eta^*|^2$ as a function of J'/γ_0 for the suspensions composed of frictionless particles at various γ_0 as indicated by the legend.

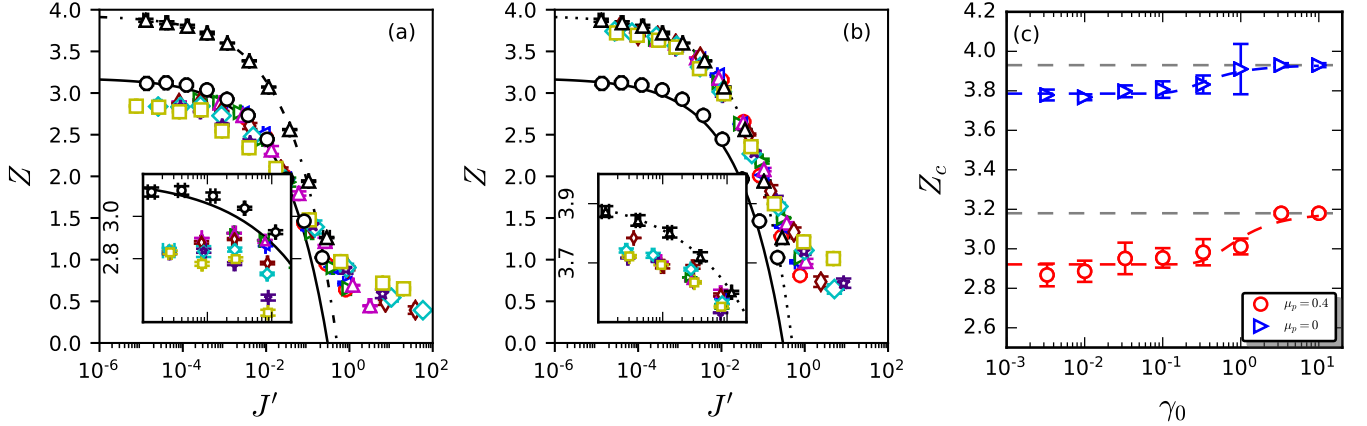


FIG. 13. The number of contacts per particle Z as a function of the viscous number J' at various γ_0 for (a) frictional and (b) frictionless suspensions. The colours and symbols are the same as in Fig. 4. The black symbols correspond to the steady-shear conditions (circles for the frictional suspensions and triangles for the frictionless suspensions), and the black lines are plots of the constitutive laws for the steady-shear cases. The constitutive laws are given as $Z = Z_c - a_Z J'^{n_Z}$, with $a_Z = 5.2$, $n_Z = 0.41$ for both the frictional and frictionless cases, $Z_c = 3.18$ for the frictional case and 3.93 for the frictionless case. The insets are the zoomed-in figures of the main figures close to $J' \rightarrow 0$. In (c) Z_c as a function of γ_0 for both the frictional and frictionless suspensions; the coloured dashed lines are best fits of the phenomenological function $Z_c = Z_c^{SS} [1 - c_1 \tanh(c_2/\gamma_0)]$, where Z_c^{SS} is the values of suspensions under steady shear with $Z_c^{SS} = 3.18$ for the frictional and $\mu_c^{SS} = 3.93$ for the frictionless cases, as indicated by the grey dashed horizontal lines. c_1 and c_2 are two fitted parameters, which values are given in the text.

We also consider an alternative contact fabric which accounts for that the shear direction reverses. This geometrical fabric measures the fabric relative to the shear direction), and which we denote as $\xi'(\theta)$, is defined as

$$\xi'(\theta) = \begin{cases} \xi(\theta), & \dot{\gamma} > 0; \\ \xi(\pi - \theta), & \dot{\gamma} \leq 0; \end{cases} \quad (14)$$

In Fig. 15 and 16, we show how the shear-rate averaged geometrical contact fabrics $\xi(\theta)$ is affected by the oscillatory shear at (a) $\gamma_0 = 10$, $\gamma_0 = 0.33$, and $\gamma_0 = 0.033$

for the suspensions composed of frictional particles at $J' \simeq 3 \cdot 10^{-3}$, without and with accounting for the shear-reversal respectively. The black lines indicate how geometrical contact fabrics would look if the suspensions behave the same as under steady-shear. The black lines in Fig. 15 are symmetrised by reflection, accounting for the shear-reversal in our system. At $\gamma_0 = 10$, the geometrical fabrics are almost identical to the steady-state both when accounting for shear-reversal direction and not. The geometrical fabrics at $\gamma_0 = 0.33$ show only a

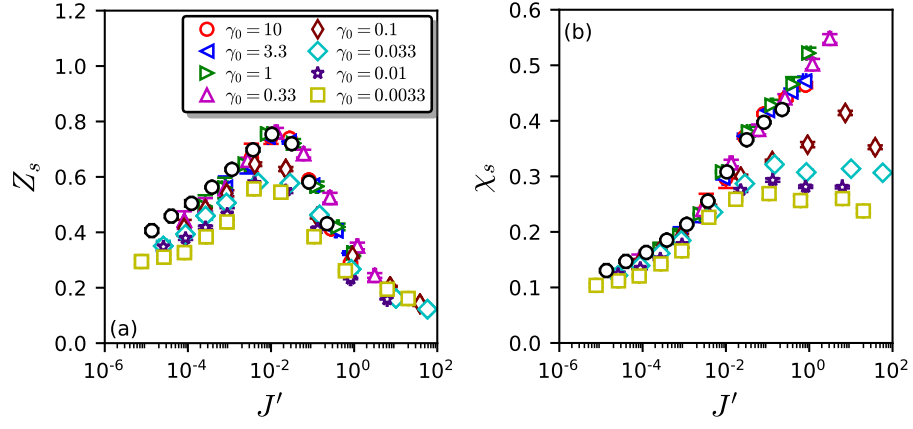


FIG. 14. (a) Number of sliding contacts per particle Z_s and (b) fraction of sliding contacts χ_s as a function of the viscous number J' at various γ_0 as indicated in the legends for the suspensions composed of frictional particles. The black symbols are data for the steady-shear.

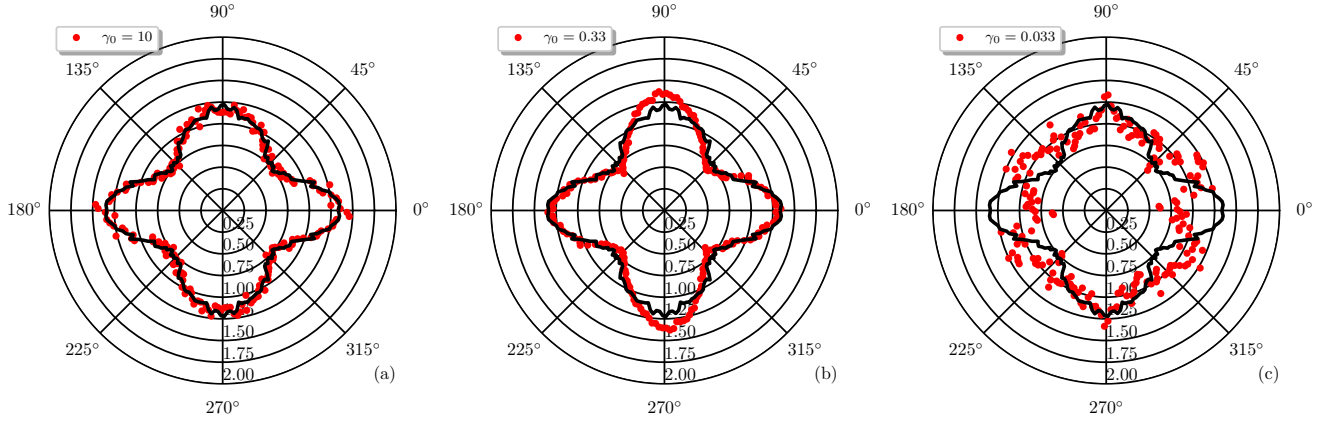


FIG. 15. The geometrical contact fabric of the suspensions composed of frictional particles at $J' \simeq 3 \cdot 10^{-3}$ and (a) $\gamma_0 = 10$, (b) $\gamma_0 = 0.33$ and (c) $\gamma_0 = 0.033$. The black lines give the steady-shear results at the same J' . The corresponding ϕ are (a) 0.770, (b) 0.797, and (c) 0.832.

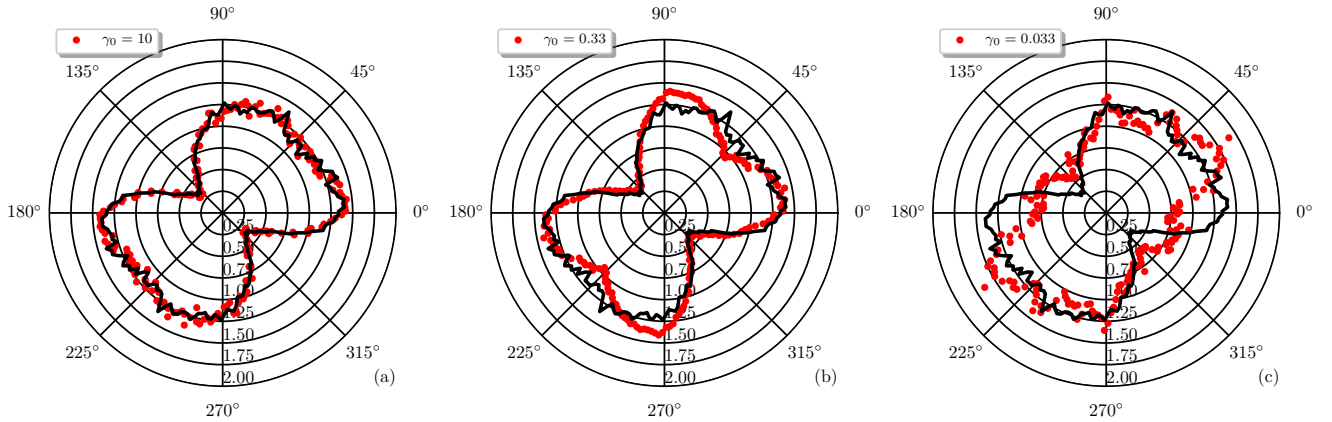


FIG. 16. The same as in Fig. 15 but along the shear direction.

minor difference than those at $\gamma_0 = 10$. As γ_0 is further lowered (at $\gamma_0 = 0.033$), the contact fabrics change from four-fold symmetry to possibly a six-fold in Fig 15. The geometrical fabric along the shear direction and at $\gamma_0 = 0.033$ is altered but remains anisotropic with high probabilities along the compression axis. The microstructure is mostly altered along the extension axis (increased probability) and the shear direction (decreased probability). Similar trends can be found for the normal and tangential fabrics and higher J' values (see the SI). In general, there is no big difference between the frictional and the frictionless cases, neither in shape nor in values, as shown in the SI.

CONCLUSIONS

In this work, we have studied the behaviour of dense suspensions composed of either frictional or frictionless particles in oscillatory shear flows at imposed pressures. We have shown that the $\mu(J)$ -rheology for non-Brownian suspensions can be generalised to oscillatory shear flows, allowing us to scan the viscoelastic properties of these suspensions in the framework a $\mu(J)$ -rheology. We found that at large strain magnitude $\gamma_0 \geq 1$, the rheological behaviour can be well-described by their corresponding rheologies in steady-shear. We interpret this as the suspensions in those cases have sufficient time to recover the steady-state microstructure at each shear-reversal. At smaller strain magnitudes, the rheology deviates from the steady-shear case (*i.e.*, does not respect the Cox-Merz rule). In both the frictional and frictionless cases, we observe a transition from a pure viscous to a viscoelastic response as strain magnitude γ_0 decreases. For both frictional and frictionless cases, we find that both the complex macroscopic friction coefficient $|\mu^*|$ and the number of contacts Z decrease compared to steady-shear for $\gamma_0 < 0.3$ and close to their corresponding shear jamming points. Although there is no clear indication of the formation of reversible states at small γ_0 [46], a consequence of our pressure imposed set-up, the lowered number of contacts and friction coefficient, as well as the increased packing fraction (frictional case), indicate that the particles partially “self-organise” or “re-organise” themselves [32 and 34], even though there is no clear signature in the contact fabric as γ_0 is lowered. As previously reported [37], the shear jamming packing fractions are found to shift to higher values at small strain magnitudes in the frictional cases, $\phi_c^{f,SS} < \phi_c < \phi_c^{nf,SS}$. This despite the fact that the fraction of sliding contacts is (mildly) lowered. For the frictionless cases, we see no significant increase in ϕ_c , although the critical number of contacts is lowered with decreasing strain amplitude. While lowering the strain amplitude yields a lower critical stress ratio and higher packing fractions (frictional case), this also leads to an emergence of elastic (or viscoelastic) behaviour. For strain amplitudes $\gamma_0 < 0.33$ we find that the shear-jamming points are elastic, while for

$\gamma_0 \geq 1$ they are viscous.

CONFLICTS OF INTEREST

There are no conflicts to declare.

ACKNOWLEDGEMENTS

MT acknowledges financial support by the Crafoord Foundation (20190650). The simulations were performed on resources provided by the Swedish National Infrastructure for Computing (SNIC) at the centre for scientific and technical computing at Lund University (LUNARC).

AUTHOR CONTRIBUTIONS

MT conceptualised the project. JD carried out the numerical simulations. JD and MT analysed the data and wrote the paper.

- [1] J. D. Ferry, *Viscoelastic properties of polymers* (John Wiley & Sons, 1980).
- [2] J. M. Dealy and K. F. Wissbrun, *Melt rheology and its role in plastics processing: theory and applications* (Springer Science & Business Media, 2012).
- [3] S. Marenne and J. F. Morris, “Nonlinear rheology of colloidal suspensions probed by oscillatory shear,” *Journal of Rheology* **61**, 797–815 (2017).
- [4] K. Hyun, M. Wilhelm, C. O. Klein, K. S. Cho, J. G. Nam, K. H. Ahn, S. J. Lee, R. H. Ewoldt, and G. H. McKinley, “A review of nonlinear oscillatory shear tests: Analysis and application of large amplitude oscillatory shear (laos),” *Progress in Polymer Science* **36**, 1697–1753 (2011).
- [5] F. Boyer, E. Guazzelli, and O. Pouliquen, “Unifying suspension and granular rheology,” *Phys. Rev. Lett.* **107**, 188301 (2011).
- [6] M. Trulsson, B. Andreotti, and P. Claudin, “Transition from the viscous to inertial regime in dense suspensions,” *Phys. Rev. Lett.* **109**, 118305 (2012).
- [7] M. Trulsson, E. DeGiuli, and M. Wyart, “Effect of friction on dense suspension flows of hard particles,” *Phys. Rev. E* **95**, 012605 (2017).
- [8] B. Andreotti, J.-L. Barrat, and C. Heussinger, “Shear flows of non-brownian suspensions close to jamming,” *Phys. Rev. Lett.* **109**, 105901 (2012).
- [9] M. Trulsson, “Rheology and shear jamming of frictional ellipses,” *J. Fluid Mech.* **849**, 718–740 (2018).
- [10] E. Irani, P. Chaudhuri, and C. Heussinger, “Impact of attractive interactions on the rheology of dense athermal particles,” *Phys. Rev. Lett.* **112**, 188303 (2014).
- [11] P. Olsson, “Dimensionality and viscosity exponent in shear-driven jamming,” *Phys. Rev. Lett.* **122**, 108003 (2019).
- [12] L. E. Silbert, “Jamming of frictional spheres and random loose packing,” *Soft Matter* **6**, 2918–2924 (2010).
- [13] M. C. Brian M. Erwin, Simon A. Rogers and D. Vlassopoulos, “Examining the validity of strain-rate frequency superposition when measuring the linear viscoelastic properties of soft materials,” *Journal of Rheology* **54**, 187 (2010).
- [14] J. Van der Werff, C. De Kruijff, C. Blom, and J. Mellema, “Linear viscoelastic behavior of dense hard-sphere dispersions,” *Physical Review A* **39**, 795 (1989).

- [15] T. Shikata and D. S. Pearson, “Viscoelastic behavior of concentrated spherical suspensions,” *Journal of Rheology* **38**, 601–616 (1994).
- [16] J. M. Bricker and J. E. Butler, “Oscillatory shear of suspensions of noncolloidal particles,” *Journal of rheology* **50**, 711–728 (2006).
- [17] Y. Lin, N. Phan-Thien, and B. C. Khoo, “Short-term and long-term irreversibility in particle suspensions undergoing small and large amplitude oscillatory stress,” *Journal of Rheology* **57**, 1325–1346 (2013).
- [18] H.-O. Park, J. M. Bricker, M. J. Roy, and J. E. Butler, “Rheology of oscillating suspensions of noncolloidal spheres at small and large accumulated strains,” *Physics of Fluids* **23**, 013302 (2011).
- [19] G. Wang and J. W. Swan, “Large amplitude oscillatory shear of hard-sphere colloidal dispersions: Brownian dynamics simulation and fourier-transform rheology,” *Journal of Rheology* **60**, 1041–1053 (2016).
- [20] A. E. H. Randy H. Ewoldt and G. H. McKinley, “New measures for characterizing nonlinear viscoelasticity in large amplitude oscillatory shear,” *Journal of Rheology* **52**, 1427 (2008).
- [21] M. Wilhelm, “Fourier-transform rheology,” *Macromolecular materials and engineering* **287**, 83–105 (2002).
- [22] K. S. Cho, K. Hyun, K. H. Ahn, and S. J. Lee, “A geometrical interpretation of large amplitude oscillatory shear response,” *Journal of rheology* **49**, 747–758 (2005).
- [23] J. Min Kim, A. P. Eberle, A. Kate Gurnon, L. Porcar, and N. J. Wagner, “The microstructure and rheology of a model, thixotropic nanoparticle gel under steady shear and large amplitude oscillatory shear (laos),” *Journal of Rheology* **58**, 1301–1328 (2014).
- [24] M. J. Armstrong, A. N. Beris, S. A. Rogers, and N. J. Wagner, “Dynamic shear rheology of a thixotropic suspension: Comparison of an improved structure-based model with large amplitude oscillatory shear experiments,” *Journal of Rheology* **60**, 433–450 (2016).
- [25] J. F. B. N. Koumakis and G. Petekidis, “Complex oscillatory yielding of model hard-sphere glasses,” *Physical Review Letters* **110**, 178301 (2013).
- [26] M. C. Lavanya Mohan, Charlotte Pellet and R. Bonnecaze, “Local mobility and microstructure in periodically sheared soft particle glasses and their connection to macroscopic rheology,” .
- [27] F. Blanc, F. Peters, and E. Lemaire, “Local transient rheological behavior of concentrated suspensions,” *Journal of Rheology* **55**, 835–854 (2011).
- [28] N. Y. Lin, B. M. Guy, M. Hermes, C. Ness, J. Sun, W. C. Poon, and I. Cohen, “Hydrodynamic and contact contributions to continuous shear thickening in colloidal suspensions,” *Phys. Rev. Lett.* **115**, 228304 (2015).
- [29] F. Peters, G. Ghigliotti, S. Gallier, F. Blanc, E. Lemaire, and L. Lobry, “Rheology of non-brownian suspensions of rough frictional particles under shear reversal: A numerical study,” *Journal of rheology* **60**, 715–732 (2016).
- [30] E. Guazzelli and O. Pouliquen, “Rheology of dense granular suspensions,” *J. of Fluid Mech.* **852**, P1 (2018).
- [31] C. Ness, Z. Xing, and E. Eiser, “Oscillatory rheology of dense, athermal suspensions of nearly hard spheres below the jamming point,” *Soft Matter* **13**, 3664 (2017).
- [32] L. Corte, P. M. Chaikin, J. P. Gollub, and D. J. Pine, “Random organization in periodically driven systems,” *Nature Physics* **4**, 420–424 (2008).
- [33] B. Metzger and J. E. Butler, “Clouds of particles in a periodic shear flow,” *Physics of Fluids* **24**, 021703 (2012).
- [34] D. J. Pine, J. P. Gollub, J. F. Brady, and A. M. Leshansky, “Chaos and threshold for irreversibility in sheared suspensions,” *Nature* **438**, 997–1000 (2005).
- [35] C. Ness, R. Mari, and M. E. Cates, “Shaken and stirred: Random organization reduces viscosity and dissipation in granular suspensions,” *Science Advances* **4**, 3 (2018).
- [36] N. Y. C. Lin, C. Ness, M. E. Cates, and I. Cohen, “Tunable shear thickening in suspensions,” *PNAS* **113**, 10774 (2016).
- [37] J. Dong and M. Trulsson, “Transition from steady shear to oscillatory shear rheology of dense suspensions,” *Physical Review E* **102**, 052605 (2020).
- [38] F. da Cruz, S. Emam, M. Prochow, J.-N. Roux, and F. Chevoir, “Rheophysics of dense granular materials: Discrete simulation of plane shear flows,” *Phys. Rev. E* **72**, 021309 (2005).
- [39] D. Ishima and H. Hayakawa, “Scaling laws for frictional granular materials confined by constant pressure under oscillatory shear,” *Physical Review E* **101**, 042902 (2020).
- [40] M. Otsuki and H. Hayakawa, “Shear jamming, discontinuous shear thickening, and fragile states in dry granular materials under oscillatory shear,” *Physical Review E* **101**, 032905 (2020).
- [41] J. Dong and M. Trulsson, “Unifying viscous and inertial regimes of discontinuous shear thickening suspensions,” *Journal of Rheology* **64**, 255–266 (2020).
- [42] M. Trulsson, E. DeGiuli, and M. Wyart, “Effect of friction on dense suspension flows of hard particles,” *Physical Review E* **95**, 012605 (2017).
- [43] M. van Hecke, “Jamming of soft particles: geometry, mechanics, scaling and isostaticity,” *Journal of Physics: Condensed Matter* **22**, 033101 (2009).
- [44] A. Singh, C. Ness, R. Seto, J. J. de Pablo, and H. M. Jaeger, “Shear thickening and jamming of dense suspensions: the roll of friction,” *Physical Review Letter* **124**, 248005 (2020).
- [45] F. Radjai, D. E. Wolf, M. Jean, and J.-J. Moreau, “Bimodal character of stress transmission in granular packings,” *Physical Review Letters* **80**, 61 (1998).
- [46] J. Dong and M. Trulsson, *in preparation*.